Ultrasound in Med. & Biol., Vol. 29, No. 11, pp. 1593–1605, 2003

0301-5629/03/$–see front matter

ELSEVIER

doi:10.1016/S0301-5629(03)01052-4

● *Original Contribution*

RADIATION-FORCE TECHNIQUE TO MONITOR LESIONS DURING ULTRASONIC THERAPY

FREDERIC L. LIZZI,* ROBERT MURATORE,* CHERI X. DENG,† JEFFREY A. KETTERLING,* S. KAISAR ALAM,* SAMUEL MIKAELIAN* and ANDREW KALISZ*

*Biomedical Engineering Laboratories, Riverside Research Institute, New York, NY, USA; and †Department of Biomedical Engineering, Case Western Reserve University, Cleveland, OH, USA

(*Received* 29 *October* 2002; *revised* 19 *June* 2003; *in final form* 15 *July* 2003)

Abstract—This report describes a monitoring technique for high-intensity focused ultrasound (US), or HIFU, lesions, including protein-denaturing lesions (PDLs) and those made for noninvasive cardiac therapy and tumor treatment in the eye, liver and other organs. Designed to sense the increased stiffness of a HIFU lesion, this technique uniquely utilizes the radiation force of the therapeutic US beam as an elastographic push to detect relative stiffness changes. Feasibility was demonstrated with computer simulations (treating acoustically induced displacements, concomitant heating, and US displacement-estimation algorithms) and pilot *in vitro* experimental studies, which agree qualitatively in differentiating HIFU lesions from normal tissue. Detectable motion can be induced by a single 5 ms push with temperatures well below those needed to form a lesion. Conversely, because the characteristic heat diffusion time is much longer than the characteristic relaxation time following a push, properly timed multiple therapy pulses will form lesions while providing precise control during therapy. (E-mail: muratore@rrinyc.org) **© 2003 World Federation for Ultrasound in Medicine & Biology.**

Key Words: **Radiation force, ARFI, Ultrasound, Lesion, Monitoring, HIFU, Elastography, PDL, Protein-denaturing lesion, Tissue ablation.**

INTRODUCTION

A number of investigators are exploring the use of high-intensity focused ultrasound (US), or HIFU, to noninvasively treat tumors and other diseases in a broad variety of organs. Potential applications include treatment of prostate hypertrophy and cancer (Sanghvi et al. 1996; Chapelon et al. 1999), breast cancer (Hynynen 1997), liver cancer (ter Haar et al. 1989) and tumors of the eye (Lizzi et al. 1999). This report addresses a novel technique for monitoring such HIFU procedures so that they can be precisely controlled to achieve optimal patient outcomes with minimal collateral damage.

HIFU produces small focal lesions mediated by the conversion of absorbed ultrasonic energy to heat. Blood flow cooling of target tissues is avoided with exposures of less than a couple of seconds (ter Haar 1995). A spatial matrix of contiguous lesions is used to treat tumors, which are typically much larger than the focal volumes of HIFU transducers. Each exposure must be sufficiently intense to induce thermal necrosis. However, in many applications, exposures must not exceed levels that produce extensive gaseous bodies through vaporization, tissue degassing or cavitation; such bodies strongly scatter US and effectively shield distal tumor elements from therapy beams (Lizzi 1993). At the lower HIFU exposures that just denature proteins, a lesion is formed that mimics the shape of the beam focal region. We term such a lesion a "protein-denaturing lesion," or PDL.

Online monitoring of HIFU lesion production is important for precisely controlling therapy and tailoring exposures to individual patients. Various monitoring approaches have been proposed. Conventional B-mode systems have permitted visualization of severe lesions, which contain strongly scattering gas bodies, but they have not provided reliable sensing of the usually desired PDLs that induce cell death without gas-body formation. Spectrum analysis has also been used to characterize subtle changes in the frequency content of ultrasonic radiofrequency (RF) echo signals. Spectrum analysis has reliably sensed tissue changes induced by ultrasonic hyperthermia, which uses moderate intensities applied for longer times (*e.g.,* 30 min) to achieve sustained tissue heating (Lizzi et al. 1997). Another ultra-

Address correspondence to: Robert Muratore, Ph.D., Riverside Research Institute, 156 William St Fl 9, New York, NY 10038-2609 USA. E-mail: muratore@rrinyc.org

sonic method involves sensing of temperature-induced changes in acoustic propagation speeds (Seip et al. 1996); this method does not directly monitor lesion production, and it can be problematic over the large temperature variations used in HIFU. Furthermore, it might not reliably show that the temperature exceeded the threshold for HIFU lesion production.

This report describes a method for monitoring thermal lesions based on their increased stiffness. Some time ago, our laboratories had qualitatively described an increased rigidity in HIFU-induced cataracts in the rabbit lens (Coleman et al. 1971). More recently, Kallel et al. (1999) have shown that ultrasonic elastography can sense and quantify changes in elastic properties associated with HIFU lesions in liver. They used off-line cross-correlation of RF echoes to image the internal deformations produced when a HIFU-treated tissue specimen was compressed using a computer-controlled large mechanical fixture. They found that the stiffness of HIFU lesions is approximately 4 times greater than that of untreated tissue; this modulus contrast depends on exposure. An acoustic emission (AE) method, described by Fatemi and Greenleaf (1998), has also been used to sense such changes. The AE method uses two incident beams with different frequencies; due to nonlinear interaction, these beams produce tissue motion where they overlap in space. The motion occurs at the difference frequency and is detected by a receiving transducer tuned to this frequency; the method has detected and mapped HIFU lesions, which alter the emissions due to perturbations in tissue absorption and stiffness (Konofagou et al. 2001).

These methods have provided useful data regarding stiffness changes, but they are difficult to implement for real-time monitoring because of the need for large mechanical elements, off-line processing (conventional elastography) and long scan time (AE). We have been investigating an alternative method that is easy to implement because it employs transducer elements already utilized in many HIFU systems. The method uses the therapy transducer to induce tissue motion *via* radiation pressure, and it employs a diagnostic US transducer to characterize this motion (Lizzi et al. 2003). We had previously described how tissue motion could be produced by radiation pressure and streaming in ocular structures *in vivo*; for example, we showed that these phenomena produce visible compression of choroidal vessels (promoting their closure) (Lizzi et al. 1981) and agitation of intravitreal masses (Coleman et al. 1980). More recently, Nightingale et al. (2001, 2002) showed that diagnostic transducers, with increased exposure levels, could produce sufficient radiation pressure to produce measurable tissue motion. A single ultrasonic transducer array is used to both apply temporally short localized radiation forces within tissue and to track the resulting displacements through time. The results indicate that acoustic radiation-force imaging (ARFI) might be capable of quantifying tissue stiffness in real-time measurements. Although this method has not been applied to lesion characterization, it has shown interesting capabilities for "remote palpation." Radiation pressure generates both compressional and shear motions; Sarvazyan et al. (1998) considered employing induced shear motion as a means to image lesions.

This report describes how our method can detect and monitor HIFU lesions by virtue of their increased stiffness. In its simplest form, the method uses a therapy transducer with a central coaxial diagnostic transducer, a transducer configuration developed in our previous ophthalmic HIFU research. A multistep procedure is employed. First, the diagnostic transducer is used to obtain A-mode RF echo data that document the initial positions of tissue elements. Then, the therapy transducer generates a short (*e.g.*, 5 ms) pretherapy pulse to induce tissue motion without modifying tissue structures. Immediately after this pulse, the diagnostic transducer is used to obtain RF echo data that are analyzed to document pretreatment tissue-motion characteristics. The therapy transducer then delivers a HIFU exposure designed to produce a thermal lesion. Next, the therapy transducer is again excited with a short motion-inducing pulse, and the diagnostic transducer is again used to track induced tissue motion. Differences in the pre- and post-HIFU motion data are used to identify lesions as regions with altered mechanical properties.

Our current initial study of this technique was designed to examine its feasibility and to clarify the roles of several key system and tissue factors. In terms of system factors, we wished to identify useful exposure levels that would induce measurable tissue displacement without producing thermal lesions. In terms of tissue factors, we wished to examine how changes in lesion stiffness affect induced motion and lesion detectability. The studies employed computer simulations for detailed investigations of these topics, followed by preliminary *in vitro* experiments to evaluate the feasibility of the method.

MATERIALS AND METHODS

Overview of methodology

Our theoretical simulations and *in vitro* experiments incorporated the transducer configuration of Fig. 1. The outer, spherical-cap transducer is similar to that used in our previous HIFU research (Coleman et al. 1986). It was fabricated from lead zirconate-titanate (PZT-4) and excited at 4.09 MHz. It had a focal length (radius of curvature) of 90 mm and an outer diameter of 42 mm. The transducer's central aperture housed a coaxial diagnostic transducer with a center frequency of 7.5 MHz, a diameter of 12.5 mm and a focal length of 60 mm. As seen in Fig. 1, the diagnostic transducer extends 30 mm

Fig. 1. Transducer configuration used in the simulations and experiments. The outer, spherical-cap transducer has a focal length of 90 mm and an outer diameter of 42 mm. A central aperture houses a coaxial diagnostic transducer with a center frequency of 7.5 MHz, a diameter of 12.5 mm, and a focal length of 60 mm. The diagnostic transducer extends 30 mm out from the apex of the therapy transducer so that the two transducers are confocal.

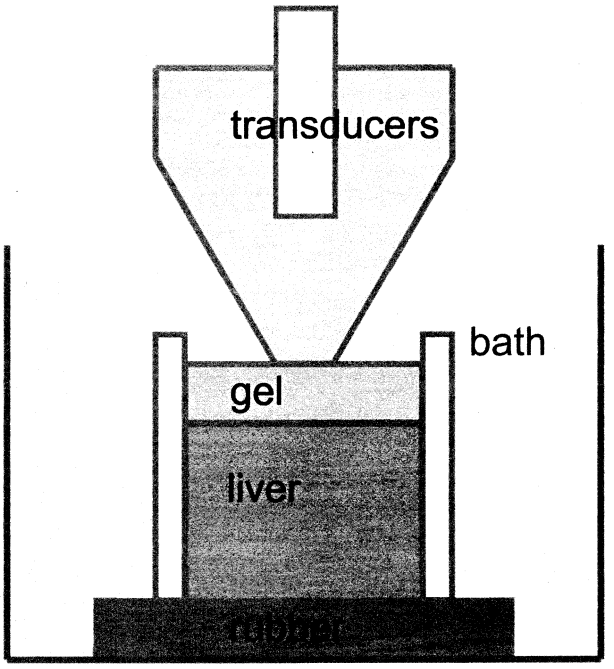

Fig. 2. Schematic diagram of experimental configuration showing fluid-filled coupling cone in contact with an aqueous gel pad. The transducers were focused near the center of a 2-cm thick degassed bovine liver tissue specimen resting on a rubber pad.

out from the apex of the therapy transducer so that the two transducers are confocal.

In operation, the central diagnostic transducer obtained initial M-mode RF data from a 1- to 2-cm region within a bovine liver specimen. The outer therapy transducer was then used in a push mode, using a brief (5-ms) pulse with a focal-point spatial-peak (SP) intensity near 1 kW/cm^2 (experimental) and 345 W/cm^2 (computational). (These values were chosen because the actual *in situ* intensity at the focus can be lower than the nominal intensity due to nonlinear propagation, a phenomenon that this study made no attempt to explore. However, the variance in the displacement is linear with intensity, as seen below in the equations of motion, eqns (1) to (3)). Within 2 ms of the end of the push, the diagnostic transducer again acquired M-mode data to determine the amplitude of tissue displacement as a function of tissue depth (range) and to track tissue recovery to initial positions. The outer transducer was then operated in a HIFU therapy mode, delivering a focused 800-ms pulse at an intensity near 3 kW/cm^2 to produce a thermal lesion. Following the HIFU exposure, M-mode data were again acquired, the push exposure was repeated, and M-mode data were obtained to follow the posttreatment extent and recovery of induced displacements. Pre- and post-HIFU M-mode results were then compared to examine motion changes attributable to lesion formation.

Computer simulation methods

Our computer simulations treated the *in vitro* experimental configuration sketched in Fig. 2. A tissue specimen (liver) was placed on a nonreflective absorbing material immersed in a water bath. The transducers of Fig. 1 were focused at a set depth (nominally 1 cm) below the tissue surface.

Three types of simulations were performed to study the major aspects of system operation. First, we computed the transient axial and radial displacements induced by a specified push exposure from the therapy transducer. Second, we used pulse-echo simulations to compute A-mode signals received from constituent liver scatterers before, during, and after the push exposure. Third, we used thermal computations to determine the spatiotemporal distribution of temperature rises induced by the push pulse. The displacement and A-mode simulations were performed for normal (untreated) liver and for liver containing a simulated thermal lesion. The simulations assumed isotropic media within each tissue type (normal and lesion), linear elastic behavior and weak acoustic scattering. They treated cylindrically symmetrical beams, as produced by the transducers in Fig. 1.

Displacement simulations. These used finite-difference algorithms to evaluate the equations of motion in tissue subjected to an internal force $\vec{F}(\vec{x})$, where the vector $\vec{x}$ specifies the three spatial coordinates of a point. Under the above conditions, with the additional assumption of local plane-waves, this internal body force arises

from gradients in radiation pressure. The value of the radiation pressure is $I(\vec{x})/c$, where $I(\vec{x})$ denotes *in situ* intensity (accounting for attenuation in intervening structures) and c is the speed of sound in the medium. We assume that scattering is weak, so the attenuation arises solely from absorption and is linearly proportional to the frequency f, with the coefficient α (Np MHz^{-1} cm^{-1}). Also, it follows from the local plane-wave condition that the internal force is directed along the propagation direction z. We neglect thermal expansion because, as we show later, the temperature rise is less than 1°C. We neglect viscosity, which we plan to include in future studies. Under these conditions, the gradient of $I(\vec{x})$ is $2\alpha f I(\vec{x})$ and the axial (sole) component of the force is

$$F_z(\vec{x}) = 2\alpha f I(\vec{x})/c. \quad (1)$$

For the cylindrically symmetric case, the induced radial and axial displacements (u_r and u_z, respectively) are described by the following equations of motion (Landau and Lifshitz 1986), written here in cylindrical coordinates:

$$\frac{\partial^2 u_r}{\partial t^2} = c_1^2\left[\frac{\partial^2 u_r}{\partial r^2} + \frac{\partial^2 u_z}{\partial r \partial z} + \frac{1}{r}\left(\frac{\partial u_r}{\partial r} - \frac{u_r}{r}\right)\right] + c_2^2\left[\frac{\partial^2 u_r}{\partial z^2} - \frac{\partial^2 u_z}{\partial r \partial z}\right] \quad (2)$$

$$\frac{\partial^2 u_z}{\partial t^2} = c_1^2\left[\frac{\partial^2 u_z}{\partial z^2} + \frac{\partial^2 u_r}{\partial r \partial z} + \frac{1}{r}\frac{\partial u_r}{\partial z}\right] + c_2^2\left[\frac{\partial^2 u_z}{\partial r^2} - \frac{\partial^2 u_r}{\partial r \partial z} + \frac{1}{r}\left(\frac{\partial u_z}{\partial r} - \frac{\partial u_r}{\partial z}\right)\right] + F_z, \quad (3)$$

where r is radial distance from the beam's central propagation axis and z is the axial distance along the beam's centerline. Equations (2) and (3) employ the following coefficients

$$c_1 = \sqrt{\frac{E(1-\nu)}{(1+\nu)(1-2\nu)\rho}}, \quad (4)$$

$$c_2 = \sqrt{\frac{E}{2(1+\nu)\rho}}, \quad (5)$$

which depend on Young's modulus, E, Poisson's ratio, ν and the density of the medium, ρ.

Our simulations first computed the free-field intensity of the therapy transducer by numerically evaluating standard diffraction integrals (O'Neil 1949). The *in situ* intensity was then computed as the free-field intensity multiplied by $\exp(-2\alpha f z_t)$, where z_t is the tissue depth at each site; the force F_z was then evaluated from eqn (1).

Table 1. Tissue parameters for liver employed in simulations.

Density	1 g mL^{-1}
Volume specific heat	4.2 J cm^{-3} $C°^{-1}$
Thermal diffusivity	0.0014 cm^2 s^{-1}
Attenuation coefficient	0.5 dB cm^{-1} MHz^{-1}; 0.06 Np cm^{-1} MHz^{-1}
Poisson's ratio	0.495
Young's modulus	
Normal	1.2 kPa
Lesion	6.0 kPa

Equations (2) to (5) were evaluated using finite-difference algorithms treating outer tissue boundaries equally with the second spatial derivative normal to the boundary set to zero, as an approximation of a nonreflective boundary. Spatial sampling was set to 0.125 mm radially and 0.5 mm axially; temporal sampling was set to 1 ns. The radial dimension of the specimen (18.5 mm) was set to be much larger than the incident beam width (0.7 mm at −3 dB) to circumvent significant edge effects during the analyzed time intervals. The tissue properties used for normal liver are listed in Table 1.

Displacement computations were performed for normal liver and for liver containing a simulated thermal lesion. The lesions were assumed to be 2 mm (radial) × 6 mm (axial) ellipsoids centered at the nominal focal point of the therapy transducer, identical to normal tissue except for their Young's modulus, which was set to 5 times that of normal liver (Table 1).

A-mode simulations. These employed the Field II US simulation program (Jensen 1996) running in MATLAB (MathWorks, Inc., Natick, MA) to compute RF echoes from a collection of point scatterers, using the diagnostic transducer parameters described above. The launched pressure-pulse waveform consisted of a Hanning-weighted 7.5-MHz sinusoidal pulse (1.5 cycles). Tissue scatterers were modeled as a 3-D spatial distribution of independent point scatterers with uniformly random positions. Scatterer density was 160 particles/mm^3. A-mode echo signals were computed using this stochastic distribution to simulate prepush echo signals. Results of the displacement simulations were then used to introduce corresponding axial and radial changes in the position of each scatterer; A-mode echo signals were then recomputed. This process was repeated for each time interval used in the displacement simulations. Motion-tracking procedures were then applied to examine detectable tissue motion during and after each push; these studies analyzed simulated A-mode signals with the same cross-correlation tracking algorithms that were used with experimental data (see below).

Thermal simulations. These were conducted to evaluate the temperature rises induced in tissue by push pulses, to determine if a single therapeutic pulse could form a lesion, and if multiple sequential therapeutic pulses could together form a lesion. These simulations employed procedures described in our previous reports (Lizzi et al. 1992). They analyzed the HIFU beam and *in situ* intensities computed for radiation pressure simulations. The absorbed dose (heat source) was computed as $2\alpha f I(\vec{x})/C$, where C is specific heat. Temperature rises were then computed using a finite-difference algorithm to evaluate the bioheat transfer equation over time and space. Spatial sampling was set to 0.05 mm radially and 0.1 mm axially; temporal sampling was set to 1 ms. (Perfusion was neglected in view of the short millisecond times of interest in this study.)

Experimental methods

Pilot experiments were conducted using degassed bovine liver specimens (room temperature), placed in an exposure container, as shown in Fig. 2. The tissue specimens had an axial length of approximately 2 cm and a width equal to the 4-cm diameter of the container. An aqueous gel pad was placed above the specimen, and a rubber absorber covered the bottom of the exposure chamber. The exposure chamber was then filled with degassed water prepared under vacuum in a magnetically stirred flask. The experiments employed the transducer assembly of Fig. 1, with an attached acrylic resin coupling cone filled with degassed water and the distal cone aperture covered with a latex rubber membrane. The whole transducer assembly was, in turn, mounted to computer controlled X-Y-Z translation stages. The assembly was then translated until the tip of the coupling cone was in contact with the gel pad.

The 42-mm diameter therapy transducer was operated at 4.09 MHz. It was calibrated using Schlieren imaging (to obtain semiquantitative beam profile data), radiation force measurements (to determine total radiated acoustic power as a function of excitation voltage) and pulse-echo reciprocity using echoes from a small glass bead (to determine the intensity distribution in the focal plane). Calibration data were used to locate the axial position of the focal point with respect to the thin membrane at the tip of the coupling cone. This information was used to position the focus at a desired depth within the liver specimen using the A-mode echo of the membrane as a reference.

The full experimental system was operated through a Microsoft Windows-based LabVIEW software interface (Microsoft Corp., Redmond, WA; National Instruments Corp., Austin, TX) that controlled motion stages, electronic signal operations and data display. A typical experiment began with a series of prepush A-scans (with a pulse-repetition rate equal to 5 kHz) of the tissue sample using a Panametrics 5900PR pulser/receiver (Panametrics, Inc., Waltham, MA). The RF echo data from the A-scan transducer was digitized with an Acqiris DP-110 (Acqiris USA, Monroe, NY) at a 500-MHz sampling rate. After acquiring the prelook A-scans, the tissue was exposed to HIFU for a fixed time duration. A gated Agilent 33250A function generator (Agilent Technologies, Inc., Palo Alto, CA) amplified by an ENI 350L broadband RF power amplifier (ENI Products division of MKS Instruments, Inc., Rochester, NY) drove the therapy transducer. The gating signal originated from a timing card in the computer and had 1-μs time resolution. Starting approximately 2 ms after the HIFU exposure, postpush A-scan data were acquired of the tissue sample. The pre- and postpush A-scan data were then combined and displayed as an M-scan image and the raw data were saved to a file.

Tissue displacements as functions of axial position and time were estimated using correlation analysis of RF data acquired before and after each push. This technique segmented each RF trace into contiguous, partially overlapping (12.5% prepush, 25% postpush) intervals and computed the correlation of each segment with a corresponding segment of prepush data. The displacement was selected from a set of candidate displacements as that which maximized the cross-correlation magnitude (Walker and Trahey 1994).

RESULTS

Simulation results

This section describes simulation results for displacements induced by a short push exposure from the therapy transducer, concomitant temperature rises and A-mode echoes with corresponding estimates of tissue displacement.

Figure 3a shows the computed free-field intensity for the therapy transducer superimposed on the target tissue; the transducer is focused 15-mm beneath the surface of the 30-mm deep tissue segment (*i.e.,* 90 mm axially distant from the transducer apex). The -3 dB points of the transducer's focal zone are computed as 0.7 mm (radial) and 17 mm (axial). Figure 3b shows the corresponding force function $F_z(\vec{x})$ computed from eqn (1). Cylindrical symmetry reduced the 3-D problem to a single plane.

Figure 4 shows the axial displacements in normal tissue induced at various times during (top row) and after (bottom row) the application of a 5-ms push pulse with a focal-point spatial-peak intensity of 345 W/cm^2. Immediately after the exposure begins, the displacement has a spatial pattern closely approximating that of the applied force (Fig. 3b), and significant motion is confined to the beam's focal zone. As time proceeds, the motion progressively spreads due to mechanical coupling. The max-

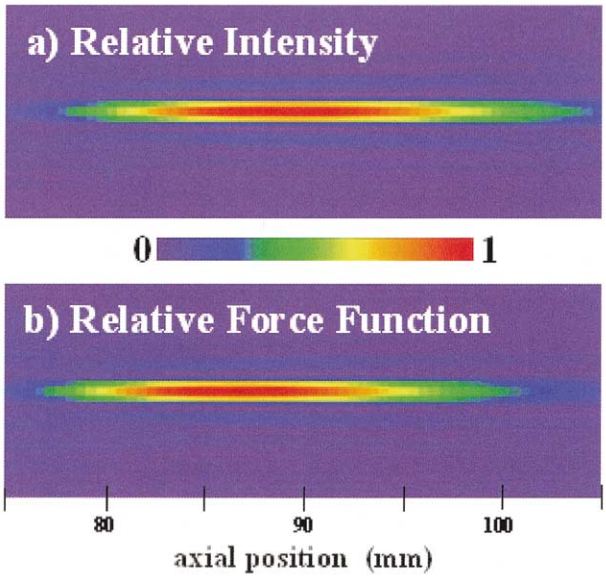

Fig. 3. Free field intensity and force function computations. As in subsequent figures, distances are specified with reference to the apex of the therapy transducer; the color bar denotes relative values of the parametric (imaged) value. The focus is at 90 mm. (a) The computed free-field intensity for the therapy transducer is superimposed on the target tissue. (b) The force function $F_z(\vec{x})$ computed from eqn (1) displays the radiation force of the incident US beam.

imum displacement is 50 μm, and it occurs near the focal point at the end of the exposure. Following the push exposure, the central region of maximal displacement rapidly returns to its initial status (zero displacement) and axial motion continues to be coupled to more distant lateral sites.

Figure 5 shows similar results for computed radial displacement; here, blue denotes motion toward the beam axis, and brown denotes motion away from this axis. Initially, the displacement pattern is determined by beam convergence. The induced motion follows the convergence of the beam in regions that are anterior to the focal plane, and it follows beam divergence beyond the focal plane. In the focal plane, radial motion is approximately zero. As time proceeds, the pattern expands in a complex fashion. The maximum radial displacement, 2.1 μm, is much smaller than the maximum axial displacement (50 μm, shown in Fig. 4).

Figure 6 shows the temperature-rise pattern induced by the push beam. Over the short time interval being studied, all temperature patterns closely resemble that of the applied beam, consistent with results of our previous reports. During the exposure, temperature increases linearly with time; it remains relatively constant at 0.26°C over the 5-ms interval following exposure. Thermal conduction, which spatially smoothes these patterns, requires longer time intervals (hundreds of ms) to become significant, and blood flow cooling can require seconds to affect temperature rises.

Figure 7 presents axial displacement results when a stiff 2 mm $\times$ 6 mm ellipsoidal lesion is present at the focal point. (The lesion was assigned a Young's modulus value 5

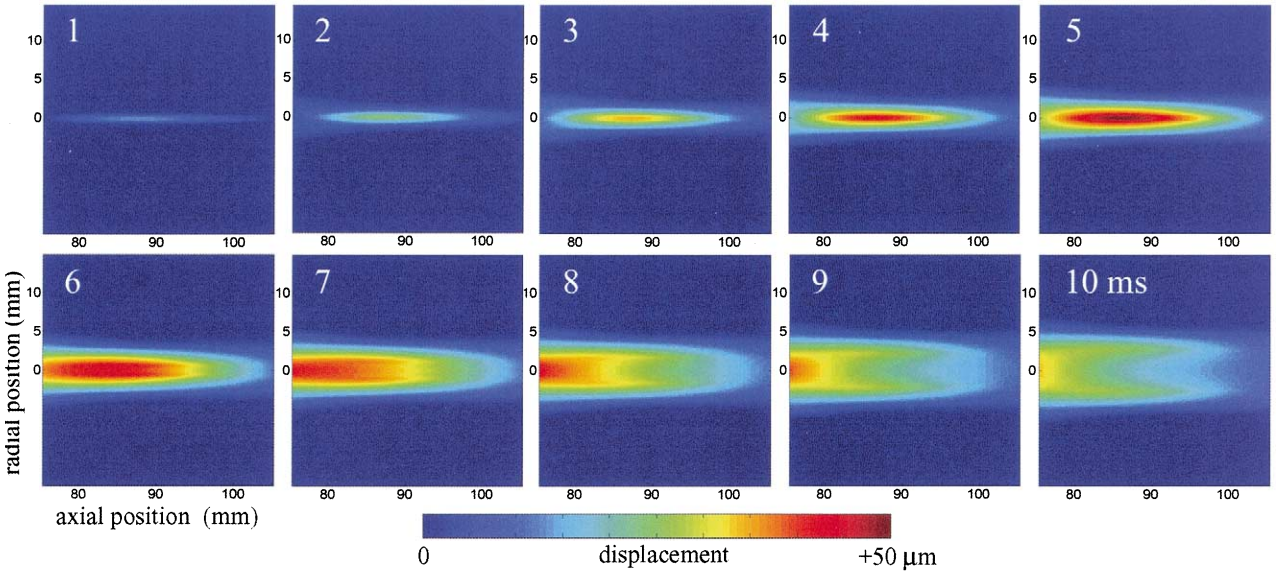

Fig. 4. Axial displacement simulations at various times, normal liver. Images show axial displacements induced at various times in normal liver during (top row) and after (bottom row) the application of a 5-ms push pulse with a focal-point spatial-peak intensity of 345 W/cm^2.

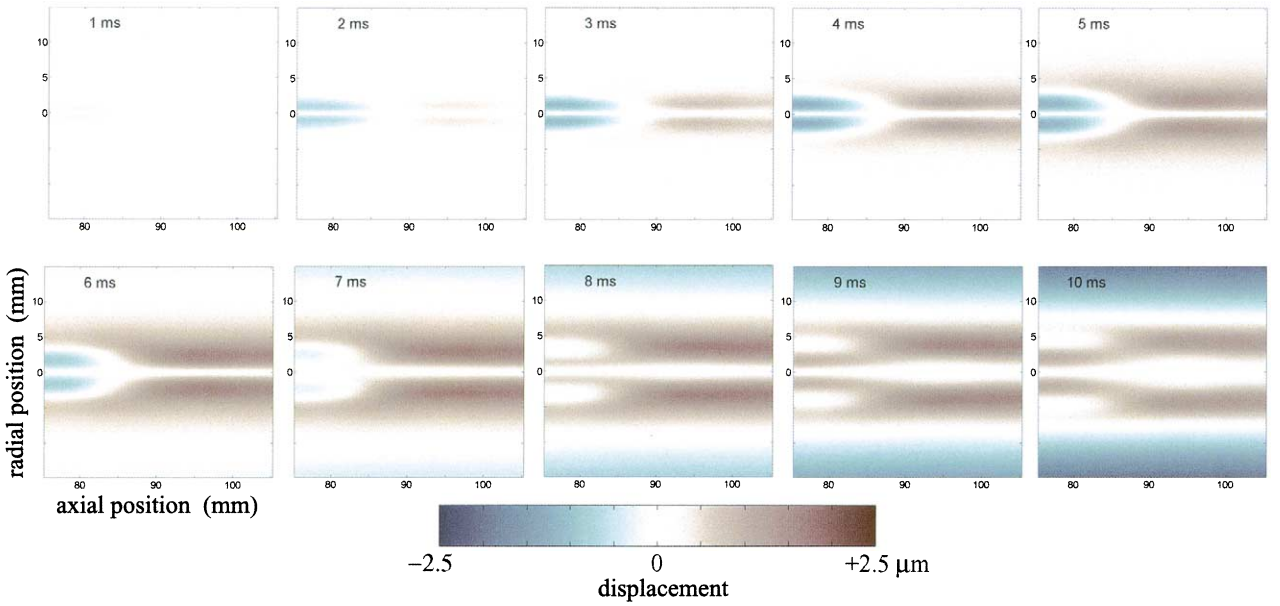

Fig. 5. Radial displacement simulations at various times, normal liver. Images show radial displacements induced at various times in normal liver during (top row) and after (bottom row) the application of a 5-ms push pulse with a focal-point spatial-peak intensity of 345 W/cm^2. Cylindrical symmetry is assumed.

times higher than surrounding normal liver, but all other properties were the same as normal liver. See Table 1.) The exposure is the same as that used above, and the force function is, again, that shown in Fig. 3. During the 5-ms push exposure, the induced displacements within the lesion are less than those at corresponding sites in normal liver (Fig. 4). The maximum displacement occurs anterior to the lesion and is 47 μm. After the pulse, axial displacement returns to zero in the center of the beam and axial motion is again coupled to more distant lateral regions.

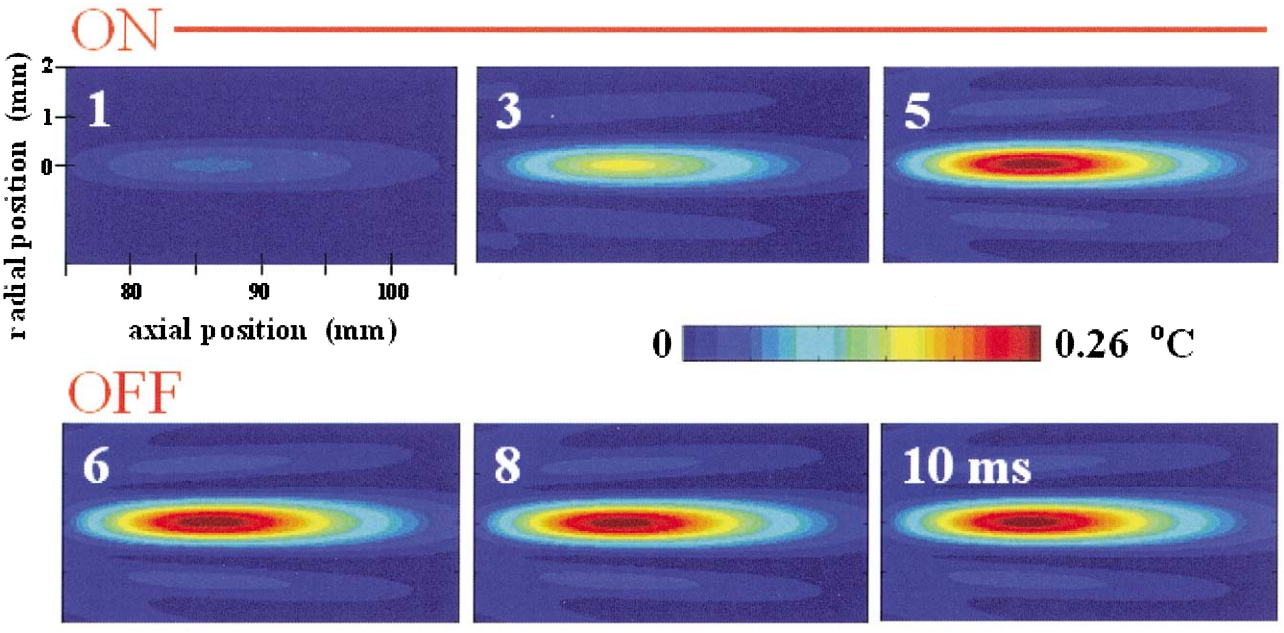

Fig. 6. Temperature rise simulations. Images show the temperature rise in the tissue due to the energy absorbed from the US push beam, used in Fig. 1, at various times.

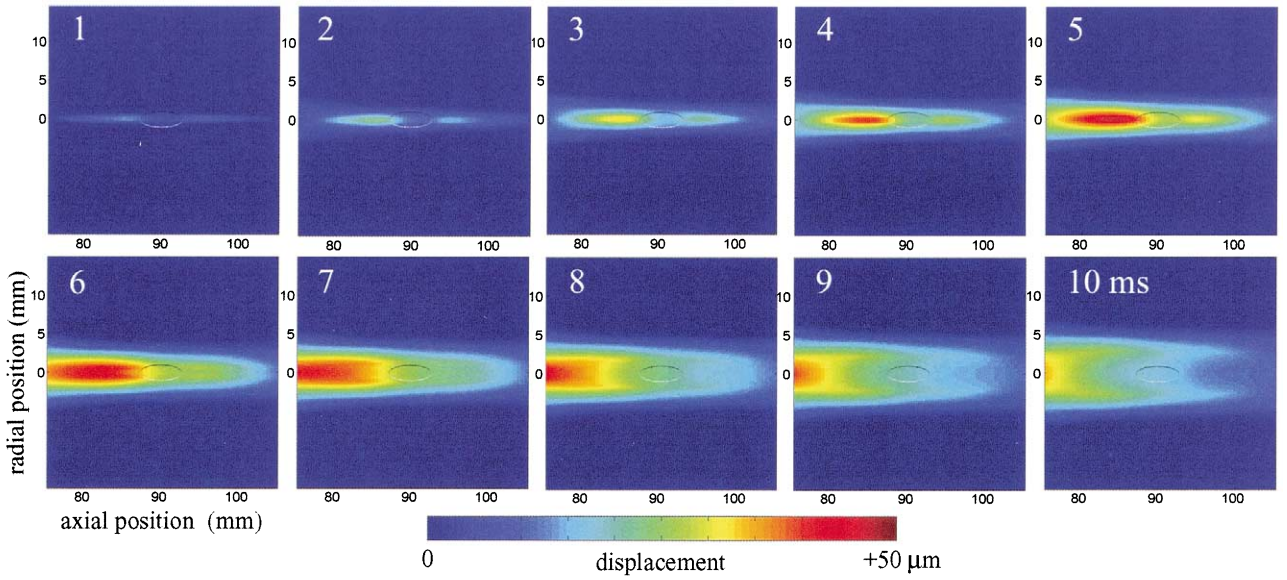

Fig. 7. Axial displacement simulations, lesion. Axial displacement results in liver are shown under the same conditions as Fig. 4, except that a stiff 2 mm × 6 mm ellipsoidal lesion is present at the focal point. The lesion was assigned a Young's modulus value 5 times higher than surrounding normal liver, but all other properties were the same as normal liver.

Figure 8 presents radial displacement results under the same conditions as Fig. 7. During the 5-ms push exposure, the induced radial displacements within the lesion are less than those at the corresponding sites in normal liver (Fig. 5). However, the maximum displacement over space is slightly greater in the presence of a lesion, 2.3 μm, than in completely normal tissue, 2.1 μm.

Figures 9 and 10 present summary results for the above simulations. Figure 9 plots the axial displacement along the beam's central axis for several time instants during the exposure. Figure 9a shows results for normal liver and Fig. 9b plots corresponding results when the thermal lesion is present. These figures demonstrate a marked reduction in induced displacement throughout the

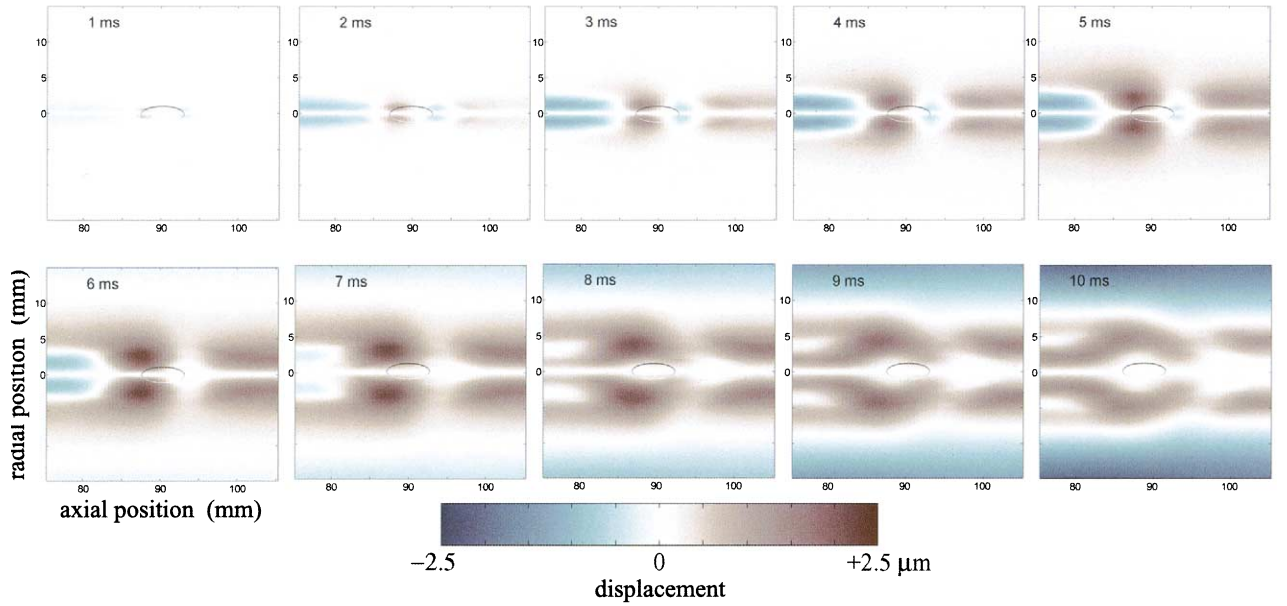

Fig. 8. Radial displacement simulations, lesion. Radial displacement results in liver are shown under the same conditions as Fig. 7.

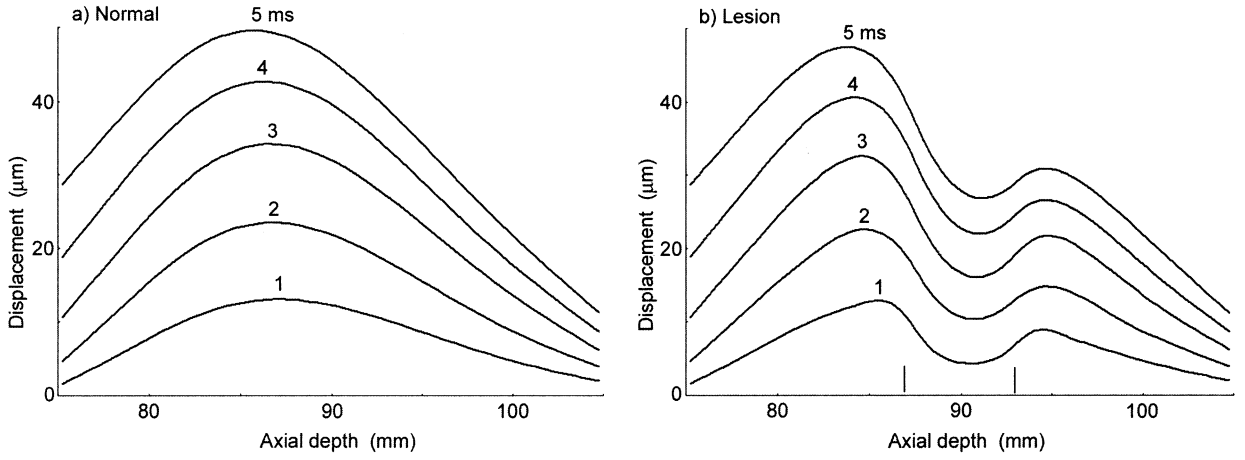

Fig. 9. Central axial-displacement graphs in (a) normal tissue and (b) lesion, under conditions used in Figs. 4 and 7, respectively. The extent of the lesion is indicated by the short vertical lines at 87 mm and 93 mm.

lesion region. Figure 10a plots focal-point displacements as a function of time for normal and lesion cases showing a rapid quasilinear rise and fall for the normal case and similar but smaller displacements when a lesion is present. Figure 10b plots the focal-point temperature for these cases; this plot pertains to both cases because no relevant thermal or acoustic parameters were changed for the lesion, which only had a different value of Young's modulus. The plot demonstrates a linear temperature rise during the exposure, and a much slower decrease after the exposure.

Figure 11 shows A-mode signals computed for a random distribution of scatterers that simulated the prepush liver. The figure also shows the A-mode signals computed at the end of the pulse, after these scatterers were spatially repositioned according to computed axial and radial displacements. The A-mode signals show several prominent features shifted to later times in the displaced tissues, as would be expected due to longer transit times. However, closer inspection shows several signal distortions presumably arising from nonuniform motion across the diagnostic beam. Figure 12 shows the corresponding displacements computed by applying our cross-correlation algorithms to the A-mode signals, such as shown in Fig. 11. These results are close to the 5-ms simulation results for normal and lesioned liver shown in Fig. 9.

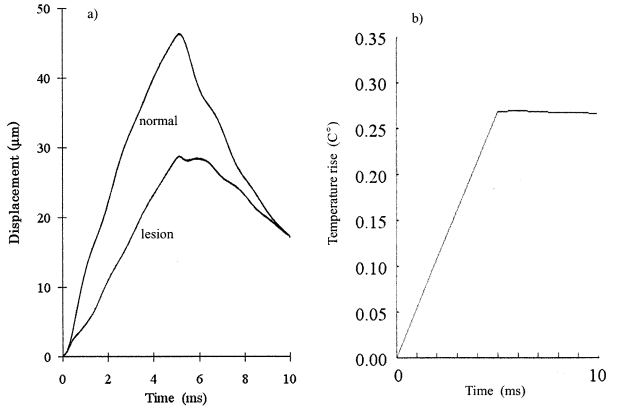

Fig. 10. Plot of graphs of (a) focal point displacement with and without lesion and (b) focal point temperature.

Experimental results

Figure 13 shows M-mode data obtained for a normal (untreated) *in vitro* liver segment before and after a push pulse from the therapy transducer. The horizontal

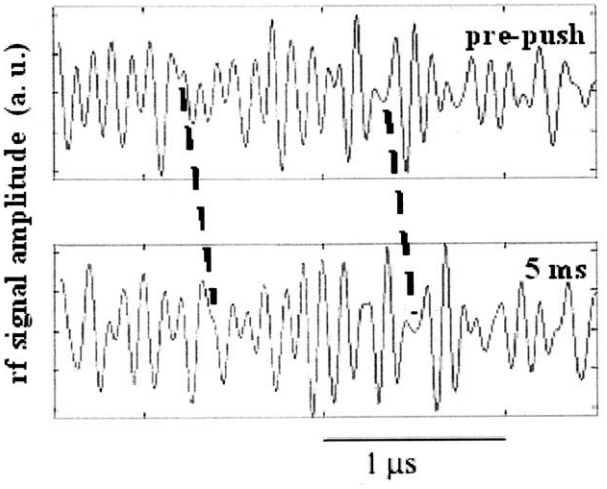

Fig. 11. Simulated RF A-mode signals before (top) and immediately after (bottom) push pulse of 5-ms duration. The portion of the RF signal shown corresponds to the backscatter from the tissue region near the focus of the pushing beam.

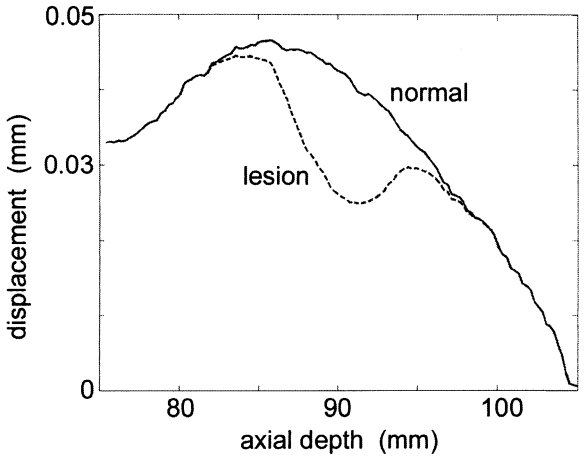

Fig. 12. Simulated displacement computations for RF data of Fig. 11, using the same cross-correlation algorithms used for experimental data.

axis represents transit time, which is proportional to tissue depth. The A-mode vertical axis represents elapsed time between A-mode examinations starting with initial observations at zero time. Grey-scale values depict the absolute values of captured RF US signals. The bright horizontal line indicates the occurrence of the 5-ms push pulse during which A-mode data acquisition was inactivated. In this display format, stationary scatterers would produce echoes that appear as straight vertical lines; horizontal deviations from these lines indicate motion. Inspection of the figures reveals small displacements to deeper sites occur following the push pulse, with subsequent recovery toward initial positions.

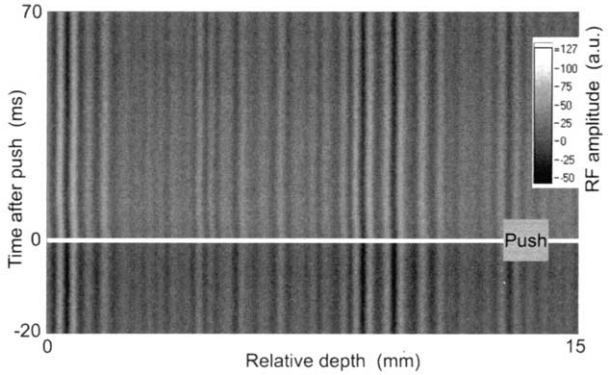

Fig. 13. Experimental M-mode data, obtained for a normal (untreated) *in vitro* liver segment before and after a push pulse from the therapy transducer. The horizontal axis represents transit time, which is proportional to tissue depth. The A-mode vertical axis represents elapsed time between A-mode examinations starting with initial observations at zero time. Grey-scale values depict the absolute values of captured RF US signals.

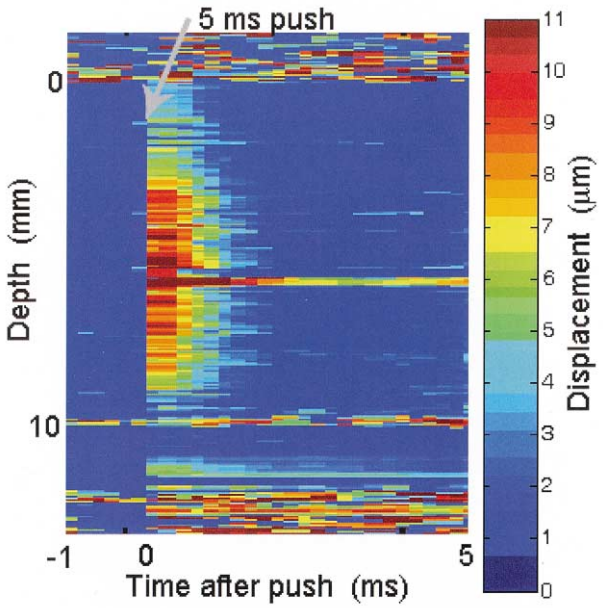

Fig. 14. Experimental displacement estimates in normal (untreated) liver specimen. Tissue depth is displayed along the vertical axis, and observation time is displayed along the horizontal axis. The bright vertical line indicates the push pulse. (The long duration horizontal bright streak might be a feature in the liver with a much longer relaxation time than the bulk of the tissue; however, it has low correlation and we treat it as artefactual.)

Figure 14 shows corresponding estimates of displacement obtained with cross-correlation algorithms. The axes are reversed in the figure so that tissue depth is displayed along the vertical axis, and observation time is displayed along the horizontal axis. This result shows noisy small displacements in the gel segment on the proximal side of the 2-cm thick liver specimen, and a decrease in signal-to-noise deep in the tissue. Following the push pulse, displacements are seen within a central segment of the specimen; these are maximal immediately after the pulse, and gradually diminish toward zero as time increases.

Figure 15 shows equivalent displacement estimates after a lesion was produced in the specimen, using the therapy transducer to deliver an 800-ms, 3 kW/cm^2 exposure. The image shows the same general displacement pattern as seen in the untreated case of Fig. 14, but it exhibits smaller displacement magnitudes.

Figure 16 was derived from data shown in Figs. 14 and 15. It plots the averaged displacement over the central 4 mm of each figure as a function of time. The plot indicates that the maximum averaged displacement (as measured starting approximately 2 ms after the end of the push, with corresponding correlation values greater than 0.9) is 15 μm for the normal specimen and 9 μm for the lesion case. In both cases, displacements return to within 1 μm of their initial values 2 ms after the start of

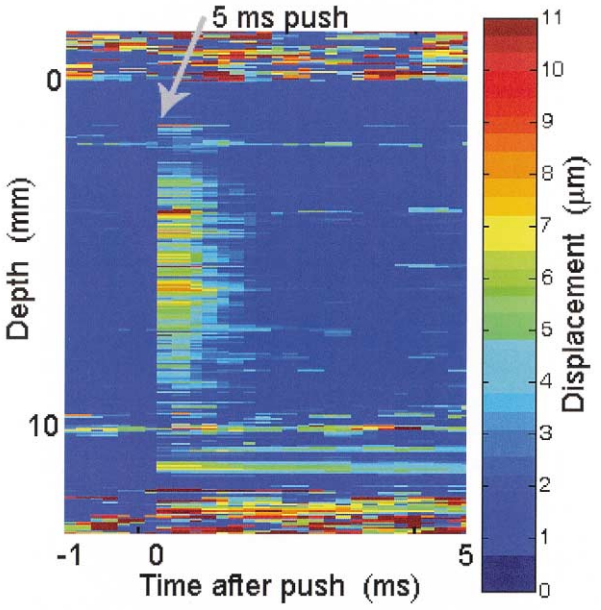

Fig. 15. Experimental displacement estimates in liver specimen with HIFU lesion.

data acquisition (approximately 4 ms after the end of the push pulse).

DISCUSSION AND SUMMARY

The results presented in this report indicate the feasibility of using displacements induced by radiation force to monitor the formation of ultrasonically induced lesions. Such lesions are of therapeutic use in the treatment of ocular, liver and other tumors and cardiac diseases. The simulations we conducted demonstrate that significant motion can be induced with short (*e.g.*, 5 ms) push exposures from HIFU transducers without the production of significant heating. They also show that these motions can be measured with colinear diagnostic transducers. In addition, the simulations showed that thermal HIFU lesions, which increase tissue stiffness, should be detected by virtue of measurable alterations in induced displacement patterns. Our pilot *in vitro* examinations were consistent with these conclusions.

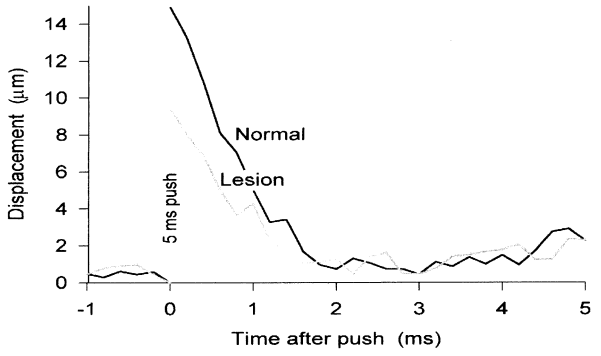

Fig. 16. Experimental displacement plots, pre- and postlesion. Displacement was averaged over the central 4 mm shown in Figs. 14 and 15, where the correlation coefficient was equal to or greater than 90%. Shown here as a function of time, normal tissue is displaced more than lesion, agreeing with the simulations shown in Fig. 10a.

This method of monitoring lesion production offers several distinct advantages. As in conventional elastography, it can sense changes in tissue properties that are difficult to detect with conventional ultrasonography. Real-time implementation is relatively straightforward and could offer a flexible and precise means for online exposure control. Push pulses and associated M-mode analysis could be interspersed at regular intervals during therapy exposures; therapy could be continued until it results in a predetermined alteration in the magnitude and spatial extent of motion characteristics indicative of the desired lesion. Imaging displacement along a set of parallel scan lines is also straightforward using, for example, a central diagnostic linear array as described in a previous report.

Derivations of Sarvazyan et al. (1998) are based on some approximations not made in our case. They ignore the compressional components of the displacement, and assume homogeneous tissue. The latter assumption means that their results can only be compared with our results for normal tissue, in which case one can see the bifurcation of the wave fronts with time in both studies (Fig. 4). The spatiotemporal variations of their force field differs from ours in slight details that do not affect the overall conclusions drawn.

The initial simulations described in this report capture the most important aspects of induced tissue motion. We are currently refining the simulation procedures by including more complete treatments of internal boundary conditions and tissue and system parameters. These improvements will permit more detailed study of subtle motion features.

The most relevant tissue property is Young's modulus, E. The simulations in this report used a modulus value cited by Chen et al. (1996) that is significantly lower than reported values for other tissues (Krouskop et al. 1998). Note that measured E values depend on experimental conditions, such as temperature, frequency, boundary conditions and operating position on the stress-strain curve. Because induced displacements decrease as E increases, we plan to measure E in a variety of relevant tissues including normal and lesioned liver specimens. In addition, we have considered only a real-valued Young's modulus, and have neglected viscosity.

Other important tissue parameters are the attenuation and absorption coefficients. As indicated in eqn (1),

these will directly affect the force function $F_z(\vec{x})$ and, thereby, influence induced tissue displacements. These coefficients are increased in HIFU lesions, leading to competing influences on the force profile that could potentially impede lesion detection by decreasing the difference in expected displacements before and after treatment. We are currently investigating these topics by parameter measurements coupled with further simulations and experiments regarding induced displacements.

Several key system factors are also being investigated. The beam width of the push beam is particularly important because it directly affects the pattern of induced motion in normal tissue. The ratio of this width-to-lesion diameter will determine whether the lesion is subjected to a broad spatially uniform force, at one extreme, or to a narrow central force, at the other extreme. The beam width of the diagnostic transducer is also important because induced displacements vary with off-axis radial distance, as can be seen in our simulation results. If the diagnostic beam is too wide, it will encompass nonuniform motion patterns that perturb postpush RF echo waveforms, changing them from initial waveforms. Such perturbations will reduce the cross-correlation amplitude used in motion tracking and, in addition, could lead to inaccurate displacement estimates. This topic will be addressed in a forthcoming paper.

Other system factors can also affect overall monitoring performance. These include push exposure parameters (frequency, intensity, duration) and diagnostic exposure parameters (frequency, pulse repetition rate). It should be noted that practical future systems need not employ the same beam pattern for push and treatment exposures. For example, the therapy transducer could comprise an annular array with one subaperture for therapy and another for inducing displacement. Alternatively, the therapy exposure could be divided into a sequence of short pulses, each of which could be followed by motion detection. In this case, our thermal simulation results show that the pulses could be placed at 10-ms intervals to obtain cumulative temperature-rise effects.

Additionally, the delay between the end of the push and the onset of data acquisition is of the same order (2 ms) as the relaxation time of the recovering displaced tissue. Therefore, our experimental technique is underestimating the maximum displacement. We plan to address this with new hardware and software.

The current simulations employed several assumptions that will be relaxed in future studies. Nonlinear propagation will affect the force function because constituent higher harmonics alter the *in situ* intensity beam pattern and the factor αf in eqn (1). Strong scattering, which is observed in severe lesions, will introduce an additional force term in eqn (1) because it involves a redirection of incident momentum. Temperature dependencies in α, c and E will also affect radiation forces and induced motion, respectively. Additionally, we plan to study the sensitivity to boundary conditions, both the normal/lesion boundary and the outer boundary. Preliminary results for different outer boundary conditions produce very similar results axially near the focus and do not appear to be a strong factor over the short times of interest. Finally, we plan to measure viscosity experimentally, and to include viscosity in future simulations.

We have not yet included all of these complex factors, limiting the precision of our current simulations. Nevertheless, the initial simulations have successfully represented the most important aspects of induced motion and have suggested specific topics for further experimental study. Future simulations promise to be a critical element in designing practical systems and properly interpreting results for precise lesion monitoring and control.

Acknowledgments—This research was supported by the National Cancer Institute (USA) and the National Heart, Lung, and Blood Institute (USA) (grant 5R01 CA84588), by the National Eye Institute (USA) (grant R01 EY10369), and by the National Cancer Institute (USA) (grant R21 CA84274).

REFERENCES

Chapelon JY, Ribault M, Vernier F, Souchon R, Gelet A. Treatment of localised prostate cancer with transrectal high intensity focused ultrasound. Eur J Ultrasound 1999;9:31–38.

Chen EJ, Novakofski J, Jenkins WK, O'Brien WD Jr. Young's modulus measurements of soft tissues with application to elasticity imaging. IEEE Trans Ultrason Ferroelec Freq Control 1996;43: 191–194.

Coleman DJ, Lizzi FL, Burt W, Wen H. Properties observed in cataracts produced experimentally with ultrasound. Am J Ophthalmol 1971;71:1284–1288.

Coleman DJ, Lizzi FL, El-Mofty AAM, Driller J, Franzen LA. Ultrasonically accelerated resorption of vitreous membranes. Am J Ophthalmol 1980;89(4):490–499.

Coleman DJ, Lizzi FL, Silverman RH, et al. Therapeutic ultrasound. Ultrasound Med Biol 1986;12:633–638.

Fatemi M, Greenleaf JF. Ultrasound-stimulated vibro-acoustic spectrography. Science 1998;280(5360):82–85.

Hynynen K. Review of ultrasound therapy. Proc IEEE Int Ultrason Sympos 1997;2:1305–1313.

Jensen JA. Field: A program for simulating ultrasound systems. Med Bio Eng Computing 1996;34(Suppl. 1):351–353.

Kallel F, Stafford RJ, Price RE, et al. The feasibility of elastographic visualization of HIFU-induced thermal lesions in soft tissues. Ultrasound Med Biol 1999;25:641–647.

Konofagou E, Thierman J, Hynynen K. A focused ultrasound method for simultaneous diagnostic and therapeutic applications—A simulation study. Phys Med Biol 2001;46:967–984.

Krouskop TA, Wheeler TM, Kallel F, Garra BS, Hall T. Elastic moduli of breast and prostate tissues under compression. Ultrason Imag 1998;20:260–274.

Landau LD, Lifshitz EM. Theory of elasticity, 3rd ed. Boston: Butterworth-Heinemann, 1986.

Lizzi FL. High-precision thermotherapy for small lesions. Eur Urol 1993;23:23–28.

Lizzi FL, Astor M, Liu T, et al. Ultrasonic spectrum analysis for tissue assays and therapy evaluation. Int J Imag Sys Tech 1997;8:3–10.

Lizzi FL, Coleman DJ, Driller J, Franzen LA, Leopold M. Effects of pulsed ultrasound on ocular tissue. Ultrasound Med Biol 1981;7(3): 245–252.

Lizzi FL, Deng CX, Lee P, et al. A comparison of ultrasonic beams for thermal treatment of ocular tumors. Eur J Ultrasound 1999;9:71–78.

Lizzi FL, Deng CX, Muratore R, et al. Radiation-force motion technique for monitoring HIFU exposures. In: Andrew MA, Crum LA, Vaezy S, eds. 2nd international symposium on therapeutic ultrasound conference proceedings 2002. Seattle, WA: CIMU, 2003: 267–274.

Lizzi FL, Driller J, Lunzer B, Kalisz A, Coleman DJ. Computer model of ultrasonic hyperthermia and ablation for ocular tumors using B-mode data. Ultrasound Med Biol 1992;18(1):59–73.

Nightingale KR, Palmeri ML, Nightingale RW, Trahey GE. On the feasibility of remote palpation using acoustic radiation force. J Acoust Soc Am 2001;110:625–634.

Nightingale KR, Soo MS, Nightingale RW, Trahey GE. Acoustic radiation force impulse imaging: *In vivo* demonstration of clinical feasibility. Ultrasound Med Biol 2002;28:227–235.

O'Neil HT. Theory of focusing radiators. J Acoust Soc Am 1949;21: 516–526.

Sanghvi NT, Fry FJ, Bihrle R, et al. Noninvasive surgery of prostate tissue by high intensity focused ultrasound. IEEE Trans Ultrason Ferroelec Freq Control 1996;43:1099–1110.

Sarvazyan AP, Rudenko OV, Swanson SD, Fowlkes JB, Emelianov SY. Shear wave elasticity imaging: A new ultrasonic technology of medical diagnosis. Ultrasound Med Biol 1998;24:1419–1435.

Seip R, VanBaren P, Cain CA, Ebbini ES. Noninvasive real-time multipoint temperature control for ultrasound phased array treatments. IEEE Trans Ultrason Ferroelec Freq Control 1996;43:1063–1073.

ter Haar G. Ultrasound focal beam surgery. Ultrasound Med Biol 1995;21:1089–1100.

ter Haar G, Sinnett D, Rivens I. High intensity focused ultrasound—A surgical technique for the treatment of discrete liver tumors. Phys Med Biol 1989;34:1743–1750.

Walker WF, Trahey GE. A fundamental limit on the performance of correlation based phase correction and flow estimation techniques. IEEE Trans Ultrason Ferroelec Freq Control 1994;41:644–654.